

See discussions, stats, and author profiles for this publication at: <https://www.researchgate.net/publication/23184665>

# Dewetting Pathways and Morphology of Unstable Thin Liquid Bilayers

ARTICLE *in* THE JOURNAL OF PHYSICAL CHEMISTRY B · SEPTEMBER 2008

Impact Factor: 3.3 · DOI: 10.1021/jp8039719 · Source: PubMed

---

CITATIONS

23

---

READS

24

## 2 AUTHORS:



[Dipankar Bandyopadhyay](#)

Indian Institute of Technology Guwahati

59 PUBLICATIONS 534 CITATIONS

SEE PROFILE



[Ashutosh Sharma IITK](#)

Indian Institute of Technology Kanpur

335 PUBLICATIONS 7,410 CITATIONS

SEE PROFILE

# Dewetting Pathways and Morphology of Unstable Thin Liquid Bilayers

Dipankar Bandyopadhyay and Ashutosh Sharma\*

Department of Chemical Engineering, Indian Institute of Technology, Kanpur 208016, India

Received: May 6, 2008; Revised Manuscript Received: June 16, 2008

Three-dimensional long-wave nonlinear analysis of the instabilities engendered by van der Waals forces in a thin ( $<100$  nm) viscous bilayer resting on a rigid substrate is presented. The bilayers are classified based on the macroscopic dewetting behavior of the films, and the three-dimensional morphological evolutions of the films are studied in each case. The dewetting of the bilayers is initiated by one of the two basic modes at the interfaces: in-phase “bending” and out-of-phase “squeezing”. We show that the thicknesses, surface energies, and viscosities of the films have significant influence on the mode selection, pathway, of dewetting, and the final morphology of dewetting. Different equilibrium morphologies are obtained by tuning the nature and the strength of the intermolecular forces present at the films, which include: (i) an array of channels and ridges in the lower layer with the upper liquid embedded inside the channels, (ii) islands in the lower layer with the upper layer embedded in the interstitial spaces, and (iii) the lower layer droplets encapsulated by the upper layer.

## Introduction

The instability and dynamics of thin ( $<100$  nm) films have been extensively studied<sup>1–51</sup> because of their importance in various products and processes, for example, in thin coatings, meso-patterning, micro- and nanofabrication, adhesives, microfluidic devices, and membranes. They also appear as the lining of mammalian lungs, as the tear film of the cornea, and in the contact region of the cell–cell or cell–substrate adhesion. These films exhibit a variety of spatio-temporal instabilities leading to either rupture or formation of a steady-state pattern. In addition to their technological and biological importance, several fundamental scientific issues such as intermolecular forces, self-organization, confinement, and finite-size effects, mesoscale dewetting, multilayer adsorption, and phase transitions can be addressed from the study of thin films. Thus, much theoretical and experimental effort has been devoted to study the instability and dewetting in thin films engendered by various intermolecular forces, most notably the long-range van der Waals force (intermolecular force).<sup>1–13</sup>

Recent studies<sup>14–26</sup> show that the surface instabilities of thin polymer bilayers may have potential applications in mesoscale patterning of polymers for optoelectronics, microelectromechanical systems, and sensor applications. The understanding of the conditions for these instabilities is also of importance because many conventional nanolithography techniques like electron beam lithography (EBL) require stable polymer bilayers. Polymer bilayers are also a simple hydrodynamic model for the adhesion of a biological membrane<sup>27,28</sup> to a solid in the presence of a surrounding liquid. Figure 1 shows the schematic diagram of the bilayer studied here. The dewetting of two immiscible layers of thin viscous (Newtonian) films on a solid substrate is interesting and complex because it involves the dynamics of two coupled deformable interfaces. The instability is initiated by selection of one of the two basic modes<sup>29</sup> of the interfacial deformations: the in-phase “bending” mode or the out-of-phase “squeezing” mode (Figure 1). Theoretical under-

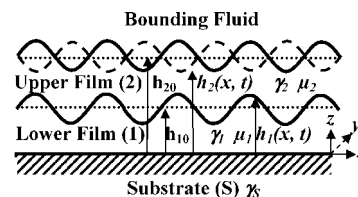


**Figure 1.** Schematic diagram of a bilayer of fluids on a solid substrate. The mean and the local thickness of the lower layer are  $h_{10}$  and  $h_1(x,t)$ , respectively. The same for the total thickness of the fluid layers are  $h_{20}$  and  $h_2(x,t)$ , respectively.  $\gamma_1$ ,  $\gamma_2$ , and  $\gamma_S$  are the surface tensions of the lower layer, upper layer, and substrate, respectively.  $\mu_2$  and  $\mu_1$  are the viscosities of the upper and lower layers, respectively. The solid and broken lines at the upper interface show a bending and squeezing mode of evolution, respectively, with respect to the lower interface.

standing of the instabilities of thin bilayer films started with a comprehensive linear and nonlinear analysis on the evaporating bilayers containing surfactants at the interfaces by Danov et al.<sup>30–32</sup> Many different aspects of the short- and long-time instabilities of viscous and isothermal bilayers have been studied.<sup>33–39</sup> In addition, several other modes of instabilities in bilayers have also been studied, such as the thermocapillarity,<sup>40–42</sup> viscoelastic materials,<sup>43,44</sup> surfactants at the interfaces,<sup>45</sup> and a confined bilayer, which is also termed as a trilayer.<sup>46</sup>

Growth of interfacial instabilities leads either to a true rupture of the film with appearances of three-phase retracting contact lines or to the formation of relatively thick precursor films connecting the liquid domains formed by dewetting.<sup>6,8,10,11,36–39,41,48–51</sup> The latter scenario of “pseudodewetting” occurs when the long-range repulsive forces<sup>6,8,11,36,37,39</sup> such as the acid–base or entropic forces are also present in addition to the destabilizing van der Waals force. It is known that, in the absence of any repulsive force, the cutoff for the van der Waals force is provided by the short-range Born repulsion,<sup>10,38,41,49–51</sup> which results in an ultrathin monolayer-like precursor film. Pototsky et al.<sup>36,39</sup> and Fisher and Golovin<sup>37</sup> studied the instability of bilayers with thick precursors where the morphology of the pseudodewetted structures is greatly influenced by the coarsening process driven by the flow through the connecting films. These studies showed

\* Author to whom correspondence should be addressed. E-mail: ashutos@iitk.ac.in.

nonlinear evolution of many interesting 2-D (two-dimensional)<sup>36,37</sup> and 3-D (three-dimensional)<sup>37,39</sup> interfacial morphologies upon changing the film thicknesses and intermolecular forces. In a previous study,<sup>38</sup> we considered the role of ultrathin precursors which result in dewetting pathways and 2-D morphologies vastly different from those obtained when thick precursors are present and true rupture is suppressed.<sup>36</sup> For example, the presence of thin precursors in the upper layer engenders secondary instabilities in the form of penetrating fronts in the lower layer, thus greatly altering the long-time evolution and morphology. Our previous work brings out the differences in the pathways of dewetting and morphological evolution in 2-D in the two cases of thick precursors<sup>36,37</sup> and true van der Waals precursors.<sup>38</sup>

The aim of this study is to uncover the dewetting pathways and corresponding dewetted 3-D morphologies of unstable van der Waals bilayers. Although 2-D simulations<sup>38</sup> can provide information on the time and length scales of the instability, at least for the early phases of growth, they cannot really differentiate even among the basic morphological phases such as droplets, holes, and labyrinths. Clearly, different morphologies have different functional aspects in a meso-pattern. We also show that the morphological evolution of the unstable bilayers with ultrathin van der Waals precursors can be entirely different compared to the case of thick precursors studied previously.<sup>39</sup> Further, we study the effects of interfacial energies, viscosities, and thicknesses of the films on the evolution of instability in a bilayer. We also explore the conditions for the formation of complex and interesting morphologies such as (i) an array of channels and ridges in the lower layer with the upper liquid embedded inside the channels, (ii) islands in the lower layer with the upper layer embedded in the interstitial spaces, and (iii) the lower layer droplets encapsulated by the upper layer. Finally, we also present the 3-D morphological evolution of bilayers for a couple of interesting configurations that have not been studied previously.<sup>39</sup> These cases are the following: (i) a completely stable upper layer on an unstable lower layer and (ii) an initially stable upper layer which becomes unstable on the solid substrate after the breakup of the lower layer. The latter phenomenon can be studied only by the use of thin precursors which allows true rupture and a contact between the upper layer and the substrate. The dewetted morphologies obtained from the simulations are compared with the available experimental<sup>18–25</sup> and theoretical studies<sup>33–39</sup> wherever it is found possible.

## Nonlinear Long-Wave Hydrodynamics

**A. Equations of Evolution for the Bilayer.** In the following section,  $x$  and  $y$  are the coordinates parallel to the substrate, the  $z$  coordinate is normal to the substrate surface (as shown in Figure 1), and  $t$  represents time. We follow the convention where the subscript  $i$  of the variable denotes the respective fluid layer ( $i = 1$  denotes the lower layer and  $i = 2$  denotes the upper layer),  $s$  denotes solid substrate, and  $g$  denotes bounding fluid (a nonviscous gas). Thus, for the layer  $i$ ,  $u_i$  is the  $x$  component of velocity,  $v_i$  is the  $y$  component of velocity,  $w_i$  is the  $z$  component of velocity,  $\mu_i$  is the viscosity,  $\rho_i$  is the density,  $\phi_i$  is the excess body force due to intermolecular interactions, and  $P_i (= p_i + \phi_i)$  is the non-bodyforce pressure in the fluid. In the expression of  $P_i$ ,  $p_i$  denotes the isotropic static pressure in the liquid. The notations  $\gamma_i$  and  $\gamma_s$  are the surface tensions of the  $i$ th fluid layer and the solid substrate, respectively. The subscripts  $t$ ,  $x$ ,  $y$ , and  $z$  in all the equations denote differentiation with respect to time and the respective coordinate. The variable composite and lower layer thicknesses are represented by  $h_2$

and  $h_1$ , respectively. Thus,  $h_3 = h_2 - h_1$  is the elastic film thickness. The notations  $h_{20}$ ,  $h_{10}$ , and  $h_{30}$  represent the respective base state thicknesses.

The long-wave equations of motion for the two layers,  $\mu_i u_{i\,zz} = (p_i + \phi_i)_x$  and  $\mu_i v_{i\,zz} = (p_i + \phi_i)_y$ , the equations of continuity for the two layers,  $u_{ix} + v_{iy} + w_{iz} = 0$ , the kinematic conditions for individual layers,  $h_{it} + u_{i|at} h_{ix} + v_{i|at} h_{iy} = w_{i|at} h_i$ , together with the equations of capillarity for the two interfaces, finally give the equations for the position of interfaces,  $h_i = h_i(x, t)$ . Since the dimensions are small, inertia is neglected. Gravity is neglected in comparison to van der Waals forces, since films are very thin ( $< 100$  nm) and thus instability due to density differences is not considered. The following boundary conditions are used:  $\mu_2 u_{2z} = 0$ ,  $\mu_2 v_{2z} = 0$  at  $z = h_2$  (zero shear at liquid–air interface);  $u_2 = u_1$ ,  $v_2 = v_1$ ,  $w_2 = w_1$ ,  $\mu_2 u_{2z} = \mu_1 u_{1z}$ ,  $\mu_2 v_{2z} = \mu_1 v_{1z}$  all at  $z = h_1$  (continuity of velocity and shear stress at liquid–liquid interface); and  $u_1 = v_1 = w_1 = 0$  at  $z = 0$  (no-slip and impermeability at the solid–liquid interface). Details of the derivation of the 2-D form are given elsewhere.<sup>35</sup> The evolution equations thus obtained shown below describe the stability, dynamics, and morphology of the liquid–air interface ( $i = 2$ ) and the liquid–liquid interface ( $i = 1$ ):

$$\frac{\partial h_1}{\partial t} - \nabla \cdot \left[ \left( \frac{h_1^3}{3\mu_1} \nabla P_1 \right) + \left( \frac{h_1^2 (h_2 - h_1)}{2\mu_1} \nabla P_2 \right) \right] = 0 \quad (1)$$

$$\frac{\partial h_2}{\partial t} - \nabla \cdot \left[ \left( \frac{(h_2 - h_1)^3}{3\mu_2} + \frac{(h_2 - h_1)h_1}{\mu_1} \left( h_2 - \frac{h_1}{2} \right) \right) \nabla P_2 + \left( \frac{h_1^2}{2\mu_1} \left( h_2 - \frac{h_1}{3} \right) \right) \nabla P_1 \right] = 0 \quad (2)$$

The total pressure at the liquid–liquid and liquid–air interface are derived from the normal stress balances at the respective interfaces as

$$P_1 = p_1 + \phi_1 = p_2 - \gamma_{12} \nabla^2 h_1 - \pi_1 \quad (3)$$

$$P_2 = p_2 + \phi_2 = p_0 - \gamma_2 \nabla^2 h_2 - \pi_2 \quad (4)$$

Here,  $p_0$  is the ambient gas pressure,  $\gamma_2$  is the surface tension of the upper layer, and  $\gamma_{12}$  is the interfacial tension at the liquid–liquid interface obtained from the relation  $[(\gamma_2)^{1/2} - (\gamma_1)^{1/2}]^2$ .<sup>47,48</sup>  $\pi_1$  and  $\pi_2$  are the van der Waals disjoining pressures at the two interfaces, which are negative of the conjoining pressures,  $\pi_i = -\phi_i$ .<sup>1–6</sup>

The disjoining pressures  $\pi_1$  and  $\pi_2$  can be written in terms of the macroscopic spreading coefficients instead of the Hamaker constants in order to make a better physical connection of the thin film instability with the macroscopic picture of wetting in the bilayer system. The equilibrium spreading coefficients,  $S_{ijk}$  denote the spreading coefficient of liquid  $i$  on material  $j$  in the presence of fluid  $k$  as the bounding (surrounding) medium. Thus,  $S_{ijk} = \gamma_{jk} - \gamma_{ik} - \gamma_{ij}$  and, when  $k$  is a gas,  $S_{ijk} = S_{ij} = \gamma_j - \gamma_i - \gamma_{ij}$ . The interfacial tensions ( $\gamma_{ij}$ ) are of the materials denoted by their subscripts ( $S$ , 1, and 2). The macroscopic equilibrium spreading coefficients used in the expressions for the potentials can also be described in terms of the effective Hamaker constants ( $A_i$ ) in the following manner:<sup>47,48</sup>

$$A_1 = A_{22} - A_{12} = -12\pi d_0^2 S_{21}$$

$$A_2 = A_{11} + A_{S2} - A_{S1} - A_{12} = -12\pi d_0^2 S_{1S2}$$

$$A_3 = A_{S2} - A_{12} = -12\pi d_0^2 (S_{1S2} - S_{1S})$$

where  $d_0$  ( $\sim 0.158$  nm) is the van der Waals equilibrium distance between the two surfaces obtained by the inclusion of the short-

range Born repulsion.<sup>49,50</sup> Thus,  $d_0$  defines the true precursor thickness of a van der Waals fluid on a solid. The binary Hamaker constants ( $A_{ij}$ ) are of the materials denoted by their subscripts (S, 1, and 2). In the notation for the indices of the effective Hamaker constant ( $A_i$ ),  $i$  does not correspond to a phase. A negative equilibrium spreading coefficient (positive effective Hamaker constant) for a single layer implies an attractive force leading to spinodal instability, and its positive value (negative effective Hamaker constant) corresponds to thermodynamic stability and perfect wetting.<sup>1–10</sup> The van der Waals disjoining pressures represented in terms of the spreading coefficients are<sup>38</sup>

$$\pi_1 = \frac{2d_0^2 S_{1S2}}{h_1^3} + \frac{2d_0^2 (S_{1S} - S_{1S2})}{(h_1 + h_3)^3} + \frac{3B_1}{h_1^4} \quad (5)$$

$$\pi_2 = \frac{2d_0^2 S_{21}}{h_3^3} + \frac{2d_0^2 (S_{1S} - S_{1S2})}{(h_1 + h_3)^3} + \frac{3B_2}{h_3^4} \quad (6)$$

Equations 5 and 6 are the simplest potentials that describe a van der Waals bilayer system. To capture the dynamics at the late stages of evolution, a short-range repulsion is included in the potential, which removes the contact-line singularity. Here, we use a “softer” repulsive potential<sup>38,51</sup> for the ease of numerical computations. The minimum of free energy occurs at a cutoff distance of  $l_0$  ( $\sim 0.137$  nm), where  $\pi_2(h_3 \rightarrow l_0) = \pi_1(h_1 \rightarrow l_0) = 0$ . The length  $l_0$  has been found to be nearly independent of the material,<sup>47,48</sup> and thus used for both of the interfaces. This magnitude of  $l_0$  is based on obtaining realistic estimates of the van der Waals components of the macroscopic parameters such as the surface tension,<sup>47,48</sup> which also ensures realistic magnitudes for the van der Waals interactions near the contact lines. These conditions finally give the following expressions for  $B_1$  and  $B_2$ :<sup>38</sup>

$$B_1 = \frac{2d_0^2 |S_{1S2}|}{3} \left[ l_0 + \frac{|N - 1|l_0^4}{(l_0 + h_3)^3} \right]; \quad B_2 = \frac{2d_0^2 |S_{1S2}|}{3} \times \left[ |P|l_0 + \frac{|N - 1|l_0^4}{(l_0 + h_1)^3} \right]$$

Here,  $N = S_{1S}/S_{1S2}$  and  $P = S_{21}/S_{1S2}$ .

### B. Nondimensional Equations and Solution Methodology.

The evolution equations (eqs 1 and 2) are nondimensionalized for a compact representation of numerical results by introducing  $X = K_1(x/h_{10})$ ;  $Y = K_1(y/h_{10})$ ;  $T = K_2(tv_1/h_{10}^2)$ ;  $H_1 = h_1/h_{10}$ ;  $H_2 = h_2/h_{10}$ ;  $M = \gamma_2/\gamma_{12}$ ;  $\bar{P}_1 = P_1 h_{10} K_1^2/\gamma_{12}$ ;  $\bar{P}_2 = P_2 h_{10} K_1^2/\gamma_{12}$ ;  $R = \mu_1/\mu_2$ ;  $N = S_{1S}/S_{1S2}$ ;  $P = S_{21}/S_{1S2}$ . The terms  $K_1 = (BC)^{1/2}$  and  $K_2 = B^2C$ , where  $B = (2d_0^2 |S_{1S2}| h_{10})/3\rho_1 v_1^2$ ,  $C = 3\rho_1 v_1^2/\gamma_{12} h_{10}$ , and  $v_1 = \mu_1/\rho_1$ .

$$H_{1T} - \nabla \cdot [H_1^3 \nabla \bar{P}_1] - \frac{3}{2} \nabla \cdot [H_1^2 (H_2 - H_1) \nabla \bar{P}_2] = 0 \quad (7)$$

$$H_{2T} - \nabla \cdot \left[ \frac{3}{2} H_1^2 \left( H_2 - \frac{H_1}{3} \right) \nabla \bar{P}_1 \right] - \nabla \cdot \left[ R (H_2 - H_1)^3 + 3(H_2 - H_1) H_1 \left( H_2 - \frac{H_1}{2} \right) \nabla \bar{P}_2 \right] = 0 \quad (8)$$

Equations 7 and 8 were discretized using a central difference scheme with half-node interpolation. The resultant sets of stiff coupled ordinary differential equations in time were solved using Gear's algorithm with an initial volume preserving random perturbation and periodic boundary conditions in space. The

grid independence of the solutions was ensured by varying the number of grid points.

## Results and Discussion

The instabilities engendered by intermolecular (van der Waals) forces in the bilayers can be apparently judged from the macroscopic spreading coefficients or the effective Hamaker constants.<sup>38</sup> For example, a bilayer with  $S_{1S2}$  and  $S_{21} < 0$  ( $A_2$  and  $A_1 > 0$ ) indicates that both the films are unstable. Again, only the lower layer can dewet the solid substrate when  $S_{1S}$ ,  $S_{1S2} < 0$ , and  $S_{21} > 0$  ( $A_2 > 0$  and  $A_1 < 0$ ). Similarly, only the upper layer dewets the lower layer when  $S_{1S}$ ,  $S_{1S2} > 0$ , and  $S_{21} < 0$  ( $A_2 > 0$  and  $A_1 < 0$ ). Equations 5 and 6 indicate that the strength of the intermolecular forces is stronger when the film thicknesses are smaller.

In what follows, the bilayers are classified into six cases<sup>35</sup> based on the surface energies of the films. The influence of surface energies, viscosities, and the film thicknesses on the dewetting behavior are demonstrated through a series of nonlinear simulations.

**A. Case 1: Bilayers on High Energy Substrates ( $\gamma_S > \gamma_1 > \gamma_2$ ).** In this case, all the spreading coefficients are positive,  $S_{1S}$ ,  $S_{2S}$ ,  $S_{21}$ , and  $S_{1S2} > 0$ . Therefore, this system is unconditionally stable as discussed elsewhere.<sup>35,38</sup>

**B. Case 2: Bilayers on High Energy Substrates ( $\gamma_S > \gamma_2 > \gamma_1$ ).** An example bilayer of this case is silicon wafer (Si)/polydimethylsiloxane (PDMS)/polystyrene (PS). The combination of surface energies ( $\gamma_S = 0.27$  N/m,  $\gamma_2 = 0.031$  N/m, and  $\gamma_1 = 0.013$  N/m) leads to  $S_{21} < 0$  and  $S_{1S2} < 0$  ( $A_2$  and  $A_1 > 0$ ), and therefore, both of the layers are unstable in this case. The destabilizing forces compete with each other, and the stronger force governs the instability. Further, the spreading coefficients  $S_{S1} > 0$  and  $S_{S2} > 0$  for this case of bilayer indicate that in the absence of the upper layer (lower layer) the lower layer (upper layer) is completely stable on the rigid substrate.

In view of the above considerations, it may be anticipated that the instability is dominated by the instability of the upper layer when it is relatively thin. Figure 2 shows the spatio-temporal evolution of such a bilayer with  $H_r = h_{30}/h_{10} = 0.5$  and  $\mu_r = \mu_2/\mu_1 = 1.0$ . In response to initial random perturbations, the interfaces of the bilayer evolve in the squeezing mode (image II) and the upper layer ruptures first because of the smaller upper layer thickness ( $h_{30} < h_{10}$ ) (image III). Here, the term “rupture” refers to the residual or the precursor thickness on the substrate being the same as the ultrathin van der Waals cutoff distance, which prevents the hydrodynamic singularity at the contact line.<sup>10,38,41,49–51</sup> In the case of thick precursors, the term “pseudodewetting” is more appropriate than “rupture”. During the initial stage of hole formation, the liquid–air interface deforms toward the surface of the lower layer and forms holes at the upper layer surface, whereas the liquid–liquid interface deforms toward the liquid–air interface and forms ridgelike structures at the surface of the lower layer (image III). Following this, the three-phase contact line around the holes moves away from the dewetted region to achieve equilibrium contact angle and the dewetted area on the lower layer increases (image IV). The growth of these holes is spatially anisotropic (images III and V) on the soft liquid–liquid interface because the deformations of the lower layer act against the retention of the basic circular shape of the holes formed in the upper layer. Further, this hole growth in the upper layer creates an area of depression adjacent to the ridges formed in the lower layer and the upper layer penetrates into the lower layer by filling out these zones of depression (image IV). In these zones, the strength of the



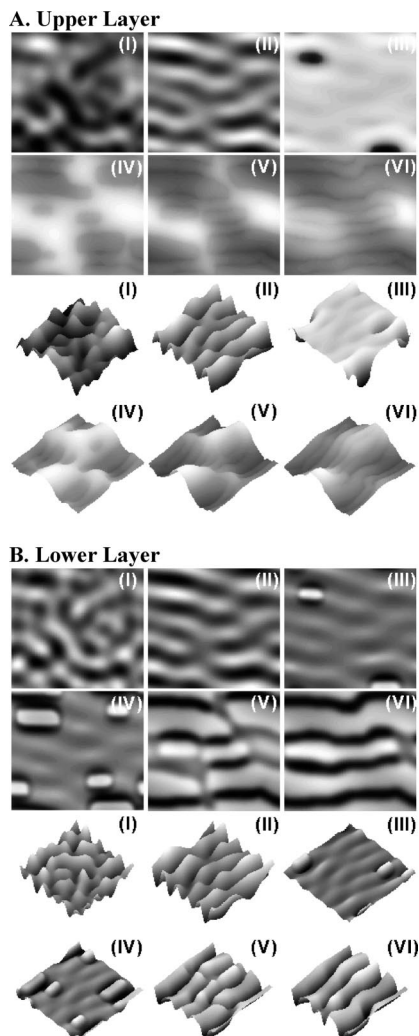


**Figure 2.** Evolution of instability in *case 2* over a  $5\Lambda_m \times 5\Lambda_m$  domain with  $h_{30} = 5$  nm,  $h_{10} = 10$  nm,  $\mu_2 = \mu_1 = 0.1$  kg/m $\cdot$ s, and  $\varepsilon_1 = \varepsilon_2 = 0.0001$ : (I)  $T = 0.00081$ , (II)  $T = 0.0036$ , (III)  $T = 0.0049$ , (IV)  $T = 0.0051$ , (V)  $T = 0.0057$ , and (VI)  $T = 0.0061$ . The darker regions in these grayscale images indicate the thinner regions.

destabilizing intermolecular force in the lower layer increases locally because of the smaller lower layer thickness. The lower layer thus ruptures within these zones of depressions (images III and IV) and exposes the solid substrate to the upper layer. At the late stages of dewetting, the lower layer progressively disintegrates into an array of ridges and channels (images IV and V). The ridges are formed in the region where the upper layer dewets the lower layer, and channels are formed at the places where the lower layer ruptures. The upper layer remains embedded inside the channels formed in the lower layer and forms a few islands on the ridges formed by the lower layer. The dewetted structures of upper and lower layer can coexist on the solid surface because, in the absence of any bounding fluid, both of the films are stable on the substrate as discussed previously.

The simulation shown in Figure 2 has a very thin, van der Waals precursor layer at the dewetted regions, and therefore, the mass transport through the intervening channels in the dewetted area is negligible. In case some interactions other than the van der Waals are present, the precursor cutoff thickness can be higher, as considered in a previous study.<sup>39</sup> It is interesting to note that the precursor thickness over the dewetted zones can have a profound influence on the spatio-temporal

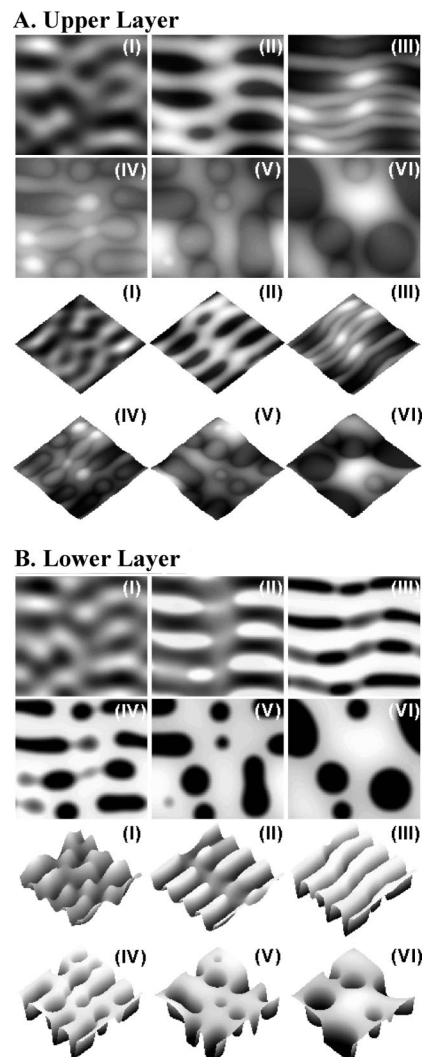


**Figure 3.** Evolution of instability in *case 2* over a  $5\Lambda_m \times 5\Lambda_m$  domain with  $h_{30} = 5$  nm,  $h_{10} = 10$  nm,  $\mu_2 = \mu_1 = 0.1$  kg/m $\cdot$ s, and  $\varepsilon_1 = \varepsilon_2 = 0.0001$ : (I)  $T = 0.0033$ , (II)  $T = 0.011$ , (III)  $T = 0.0128$ , (IV)  $T = 0.0147$ , (V)  $T = 0.02$ , and (VI)  $T = 0.0368$ . The darker regions in these grayscale images indicate the thinner regions.

evolution and resulting morphologies. For example, Figure 3 shows the evolution of the same bilayer as shown in Figure 2 but with a higher precursor film thickness connecting the dewetted structures. As in the previous case, images I and II show that initially the interfaces again evolve in squeezing mode and the first rupture takes place in the upper layer. Subsequently, the ridgelike structures appear on the lower layer surface after the upper layer ruptures (image II) and the zone of depression created adjacent to the dewetted zone in the upper layer grows to form holes in the lower layer (image III). It may be noted that, in this case of a thicker precursor, the sharp features near the contact line are absent, and consequently, incursion of the upper layer into the lower layer and the subsequent ruptures (image III of Figure 2) in the lower layer do not develop. Following the ruptures in the upper and lower layers, the growth of the dewetted regions and the coalescence of the structures (image IV) takes place simultaneously to form cavities in the lower layer (image V). The upper layer fills up these cavities together with the formation of some islands on the lower layer (images V and VI). Long-time morphology in image VI shows that these microcavities can further coalesce to form larger cavities in the lower layer. Thus, a comparison of Figures 2 and 3 clearly demonstrates the important role of precursor

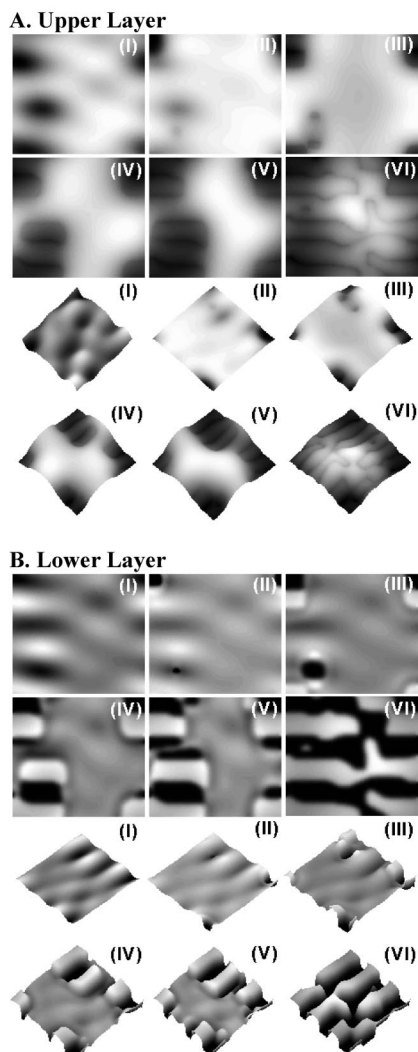


**Figure 4.** Evolution of instability in *case 2* over a  $3\Lambda_m \times 3\Lambda_m$  domain with  $h_{30} = h_{10} = 10$  nm,  $\mu_2 = \mu_1 = 0.01$  kg/m $\cdot$ s and  $\varepsilon_1 = \varepsilon_2 = 0.001$ : (I)  $T = 0.072$ , (II)  $T = 0.074$ , (III)  $T = 0.075$ , (IV)  $T = 0.0766$ , (V)  $T = 0.077$ , and (VI)  $T = 0.0827$ . The darker regions in these grayscale images indicate the thinner regions.

thickness in the dewetting mechanism and resulting morphologies, which are markedly different in the two cases. The morphologies of Figure 3 resemble the results presented recently by Pototsky et al.<sup>39</sup> using a similar set of conditions ( $H_r = 0.5$  and  $\mu_r = 1.0$ ) and relatively thick precursors.

The dewetting pathway shown in Figure 2 can significantly change if the relative strength of the intermolecular forces is altered by tuning the film thicknesses. Figure 4 shows the dewetting of a bilayer with a thicker upper layer ( $H_r = 1.0$ ) as compared to the bilayer discussed in Figure 2 ( $H_r = 0.5$ ). The figure shows that the instability is initiated by the bending mode of deformation at the interfaces and the stronger destabilizing intermolecular force in the lower layer causes first rupture at the lower layer (image II). Thereafter, the holes formed in the lower layer grow wider because of the uncompensated Young's force arising from the dynamic contact angle being different from the equilibrium contact angle. Consequently, the growth of the rim height adjacent to the holes leads to local thinning of the upper film and the upper layer dewets the lower layer at the crest of the rims because of the stronger local destabilizing intermolecular force (images II and III). Image IV shows that, as the holes formed in the upper layer grow wider, the upper

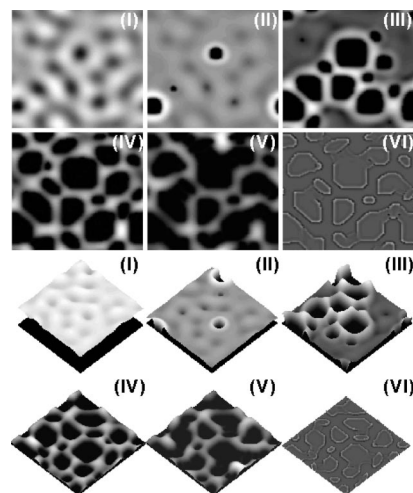


**Figure 5.** Evolution of instability in *case 2* over a  $5\Lambda_m \times 5\Lambda_m$  domain with  $h_{30} = h_{10} = 10$  nm,  $\mu_2 = 0.001$  kg/m $\cdot$ s,  $\mu_1 = 1$  kg/m $\cdot$ s, and  $\varepsilon_1 = \varepsilon_2 = 0.001$ : (I)  $T = 0.0081$ , (II)  $T = 0.0087$ , (III)  $T = 0.0093$ , (IV)  $T = 0.0099$ , (V)  $T = 0.011$ , and (VI)  $T = 0.011$ . The darker regions in these grayscale images indicate the thinner regions.

layer fluid penetrates into the lower layer in the space adjacent to the holes formed in the upper layer. At these spots, the lower layer becomes thinner and the locally strong destabilizing intermolecular force causes further ruptures in the lower layer (images IV and V). Near equilibrium, the lower layer disintegrates into an array of channels and ridges (image VI). The upper fluid remains embedded in the channels formed in the lower layer. It is interesting to note that, although the location of the first rupture is different, similar dynamics of evolution in the nonlinear regime leads to final morphologies that closely resemble structures in Figures 2 and 4.

Apart from the intermolecular forces, the viscous forces also play a major role in determining the dewetting pathway because it can influence the kinetics of destabilization. Elsewhere,<sup>38</sup> we showed that a relatively high viscosity in the upper layer slows down the overall rate of bilayer dewetting because it impedes the growth rate of the deformations at both of the interfaces. The dewetting pathway in such systems remains similar to the examples shown in Figures 2 and 4 depending upon which one of the layers ruptures first. In contrast, a completely different dewetting pathway is observed when the upper layer is less viscous to the extent that it can break up at a faster rate than the lower layer. Figure 5 shows the evolution of a bilayer with similar film thicknesses as described in Figure 4, but with increased viscosity of the lower layer ( $\mu_1$  to 1.0 kg/m $\cdot$ s) and decreased viscosity of the upper layer ( $\mu_2$  to 0.001 kg/m $\cdot$ s). The change in the relative viscosities of the films changes the relative kinetics of destabilization of the two layers. In contrast to the dewetting pathway shown in Figure 4, initial evolution occurs by the squeezing mode rather than the bending mode and the first rupture now takes place in the upper layer (image II). Although the thickness ratio corresponds to a stronger destabilizing intermolecular force for the lower layer, the lower viscous resistance of the upper layer ensures that it ruptures first in a short time. Thereafter, the holes formed in the upper layer grow spatially because of the uncompensated Young's force and a number of satellite holes appear adjacent to the rims of these holes (image III). Further, the dewetted regions grow and the upper layer liquid forms a polygonal networklike structure on the lower layer (image IV). At the late stages of evolution, the upper layer disintegrates into ribbonlike structures along with a few isolated droplets (image V). The interfacial

morphology at the liquid–liquid interface in image VI shows that the structures formed in the upper layer (image V) do not show significant incursions into the highly viscous lower layer, but a weak replica of the upper interface is formed on the lower liquid–liquid interface.

There seems to be no experimental studies involving thin viscous bilayers where the lower layer is less viscous. Experimental studies with the bilayers having a less viscous upper layer are more common, and our simulations show similarity in the interfacial morphologies when compared with the existing experimental works. Dewetted structures similar to that shown in image III of Figure 5 for the less viscous upper layer are observed in Figure 4 of Lin et al.,<sup>17</sup> Figure 2 of Pan et al.,<sup>19</sup> Figure 2 of Segalman et al.,<sup>20</sup> and in Figures 1 and 2 of Kang et al.<sup>22</sup> In addition, the polygonal structures shown in Figure 5 of Segalman et al.<sup>20</sup> are quite similar to the morphologies obtained in image IV of Figure 5. The islands of droplets and ribbonlike structures shown in image V are also reported by Wunnicke et al.<sup>23</sup> in Figure 1 of their work. Further, the penetration of the less viscous upper layer in the more viscous lower layer as shown in image VI is also observed by Lambooy et al.,<sup>18</sup> Segalman et al.,<sup>20</sup> and Li et al.<sup>25</sup> while studying different polymer bilayer systems.

**C. Case 3: Bilayers on Low Energy Substrates ( $\gamma_S < \gamma_1 < \gamma_2$ ).** An example of this case is SiO<sub>2</sub>/PS/PMMA ( $\gamma_S = 0.026$  N/m,  $\gamma_2 = 0.036$  N/m, and  $\gamma_1 = 0.031$  N/m) where SiO<sub>2</sub> is quartz and PMMA is polymethylmethacrylate. Attractive intermolecular forces because of  $S_{1S} < 0$  and  $S_{21} < 0$  ( $A_{1S}$  and  $A_1 > 0$ ) both govern the instability in this case. The upper layer destabilization is further aided by  $S_{21} < 0$ . The force due to  $S_{1S2} > 0$  ( $A_2 > 0$ ) contributes to the lower layer stability, but  $S_{1S} < 0$  can cause its destabilization. The lower layer is thus initially weakly unstable.

Figure 6 shows the evolution of instability of a bilayer with equal thickness and viscosities ( $H_r = \mu_r = 1$ ). At short time, the squeezing mode of deformation prevails at the interfaces (image II). The stronger destabilizing intermolecular force in the upper layer leads to the rupture of the upper layer first. Ridgelike structures are formed on the surface of the lower layer at the zones where the upper layer dewets the lower layer (image III). The ridges on the surface of the lower layer (holes in the upper layer) grow in size as the three-phase contact line moves to achieve the equilibrium. The growth of the dewetted regions in the upper layer creates a zone of penetration surrounding the ridges on the lower layer (image III), and the lower layer becomes thinner in these places locally. Consequently, under the influence of the weak destabilizing intermolecular force present in the lower layer ( $S_{1S} < 0$ ), an incomplete dewetting of the lower layer on the solid takes place from the locally thin regions in the lower layer (image IV). The dewetting is incomplete because the stabilizing van der Waals repulsion ( $S_{1S2} > 0$ ) acts against the destabilizing intermolecular interaction ( $S_{1S} < 0$ ) present in the lower layer and never allows the upper layer to meet the solid substrate. We term the incomplete dewetting of the lower layer liquid on the solid as “frustrated dewetting”<sup>38</sup> because the dewetting in the lower layer is always associated with a relatively thick precursor. Images III and IV also show that, during the frustrated dewetting, a number of new ridges appear at the locations where the upper layer dewets the lower layer and, simultaneously, the old ridges grow in size. Rapid coarsening of the ridges results from the fast flow of liquid through the intervening thick precursor films. Late stages of evolution show coalescence of the ridges formed on the lower layer surface (images V and VI). Finally, the upper layer remains

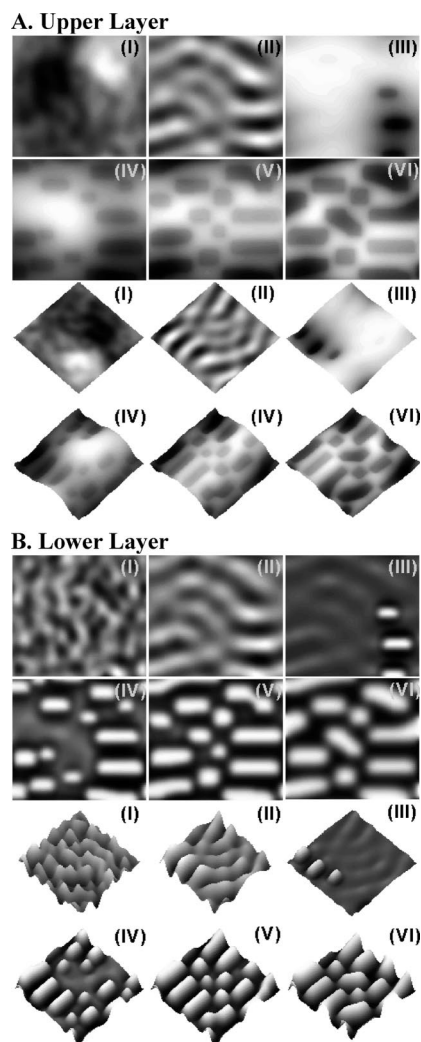


**Figure 6.** Evolution of instability in case 3 over a  $5\Lambda_m \times 5\Lambda_m$  domain with  $h_{30} = h_{10} = 10$  nm,  $\mu_2 = \mu_1 = 1$  kg/m<sup>2</sup>s, and  $\varepsilon_1 = \varepsilon_2 = 0.001$ : (I)  $T = 0.00185$ , (II)  $T = 0.039$ , (III)  $T = 0.056$ , (IV)  $T = 0.063$ , (V)  $T = 0.068$ , and (VI)  $T = 0.107$ . The darker regions in these grayscale images indicate the thinner regions.

embedded inside the interstitial spaces between the ridges formed on the surface of the lower layer and the lower layer disintegrates into an array of ridges and channels (image VI). Unlike case 2 discussed earlier, the upper layer always rests on a cushion of lower layer because of the frustrated or incomplete dewetting of the lower layer.<sup>38</sup>

**D. Case 4: Bilayers on Low Energy Substrates ( $\gamma_S < \gamma_2 < \gamma_1$ ).** An example of this kind of bilayer is SiO<sub>2</sub>/PMMA/PS ( $\gamma_S = 0.026$  N/m,  $\gamma_2 = 0.031$  N/m, and  $\gamma_1 = 0.036$  N/m). In this case, the spreading coefficients are  $S_{21} > 0$  ( $A_1 > 0$ );  $S_{1S}$ ,  $S_{2S}$ , and  $S_{1S2} < 0$  ( $A_{1S}$ ,  $A_{2S}$ , and  $A_1 > 0$ ). The lower layer is unstable under the influence of  $S_{1S2} < 0$  ( $A_2 > 0$ ) and  $S_{1S}$  ( $A_{1S} > 0$ ). The upper layer is stable because  $S_{21} > 0$  but becomes unstable when it comes in contact with the solid because of  $S_{2S} < 0$ . This opens up an interesting possibility of the formation of secondary structures by dewetting of the upper layer on the solid once the lower layer ruptures. This is shown in the example below.

Figure 7 shows the evolution of instability in a bilayer with  $H_r = 0.5$  and  $\mu_r = 1$ . Image I shows that in response to the initial random perturbation, the interfaces initially evolve in the bending mode and because of the strong destabilizing intermolecular interaction the initial rupture takes place at the lower



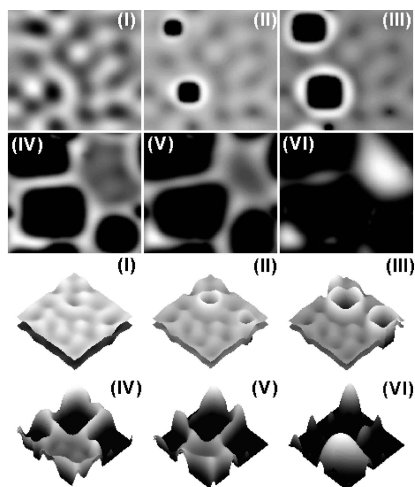


**Figure 7.** Evolution of instability in *case 4* over a  $4\Lambda_m \times 4\Lambda_m$  domain with  $h_{30} = 5$  nm,  $h_{10} = 10$  nm,  $\mu_2 = \mu_1 = 0.1$  kg/m $\cdot$ s, and  $\varepsilon_1 = \varepsilon_2 = 0.05$ : (I)  $T = 0.687$ , (II)  $T = 0.884$ , (III)  $T = 0.93$ , (IV)  $T = 1.04$ , (V)  $T = 1.12$ , and (VI)  $T = 1.4$ . The darker regions in these grayscale images indicate the thinner regions.

layer. This brings the upper layer in contact with the solid, and under the influence of  $S_{2S} < 0$ , the upper layer now also dewets the solid (image II). Interestingly, the equilibrium contact angle ( $\theta_1$ ) of the dewetting front resulting from the rupture of the lower layer on the solid in the presence of the upper layer is smaller than the equilibrium contact angle ( $\theta_2$ ) forming from the upper layer rupture on the solid substrate in the air. This is because  $|S_{2S}| > |S_{1S2}|$ . Therefore, as the hole formed in the lower layer grows to achieve the equilibrium contact angle (image III), the dewetting front created after the dewetting of the upper layer on the solid forces the contact line of the ruptured lower layer to recede beyond its equilibrium. In this process, the upper layer encapsulates the lower layer. The eventual size of the holes formed in this case becomes much larger than the linear length scale of the instability (image IV). At the late stages of dewetting, both of the films form polygonal networklike structures (images IV and V). Finally, the liquid bridges of the polygonal network break and encapsulated droplets are observed on the substrate surface. Simultaneous dewetting of both of the layers on the low energy substrate exposes it to air in the places where droplets are absent.

**E. Case 5: Bilayers on Intermediate Energy Substrates** ( $\gamma_1 > \gamma_s > \gamma_2$ ). An example of this case is SiO $_2$ /PS/PDMS ( $\gamma_s = 0.026$  N/m,  $\gamma_2 = 0.013$  N/m, and  $\gamma_1 = 0.031$  N/m). The spreading coefficients are  $S_{21}$  and  $S_{2S} > 0$  ( $A_1$  and  $A_{2S} < 0$ );  $S_{1S}$  and  $S_{1S2} < 0$  ( $A_{1S}$  and  $A_2$  and  $< 0$ ). Thus, the instability is caused by the attractive components,  $S_{1S}$  and  $S_{1S2}$ . From the free energy point of view, the only difference with *case 4* is that  $S_{2S} > 0$ , which ensures the stability of the upper layer on the solid substrate after the rupture of the lower layer.

Figure 8 shows the evolution of instability in a bilayer with  $H_r = 0.5$  and  $\mu_r = 1$ . In this case, the interfaces evolve in the bending mode in the beginning and the lower layer ruptures (image II) under the influence of a destabilizing intermolecular force. In image II, depressions appear in the upper layer because the upper layer liquid descends to fill up the holes formed in the lower layer. The holes in the lower layer grow (image III), and the dewetted area increases. At this stage, some satellite holes appear from the zones of depression adjacent to the rims of the primary holes (images IV and V). Finally, the bilayer shows ribbonlike morphologies along with some isolated droplets (image VI). The combination of surface energies for

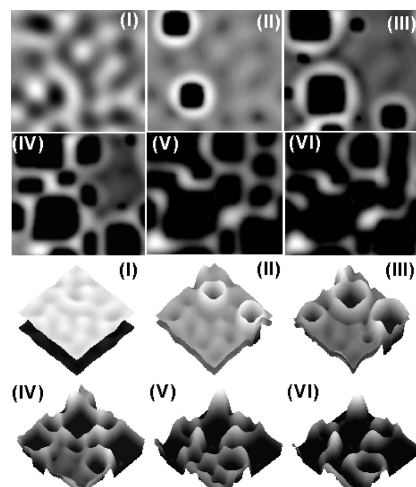


**Figure 8.** Evolution of instability in *case 5* over a  $4\Lambda_m \times 4\Lambda_m$  domain with  $h_{30} = 5$  nm,  $h_{10} = 10$  nm,  $\mu_2 = \mu_1 = 0.1$  kg/m $\cdot$ s, and  $\varepsilon_1 = \varepsilon_2 = 0.05$ : (I)  $T = 0.097$ , (II)  $T = 0.17$ , (III)  $T = 0.187$ , (IV)  $T = 0.199$ , (V)  $T = 0.218$ , and (VI)  $T = 0.247$ . The darker regions in these grayscale images indicate the thinner regions.

this case ensures that the upper layer is stable on both the rigid substrate and the lower layer. Thus, in contrast to *case 4* discussed earlier, the dewetted substrate and the equilibrium structures formed in the lower layer are always covered with a thin cushion of the upper layer liquid. Our recent experiments (unpublished) for thin PS/PDMS bilayers show final morphologies similar to image VI.

**F. Case 6: Bilayers on Intermediate Energy Substrates** ( $\gamma_2 > \gamma_s > \gamma_1$ ). An example of this case is SiO $_2$ /PDMS/PS ( $\gamma_s = 0.026$  N/m,  $\gamma_2 = 0.031$  N/m, and  $\gamma_1 = 0.013$  N/m). The nonlinear evolution, influences of film thicknesses and viscosities, and the morphologies generated were all found to be similar as in *case 2* discussed previously. The signs of the spreading coefficients ( $S_{1S} > 0$ ;  $S_{1S2}$ ,  $S_{2S}$  and  $S_{21} < 0$ ) show that both of the films are unstable in this case, as in *case 2*, and therefore, the qualitative features of the evolution and their underlying mechanisms are also similar to those explained for Figures 2 and 4 at low and high  $H_r$ , respectively. The influence of the liquid viscosities was also found to be similar, as discussed for *case 2*.

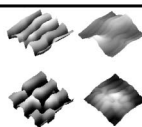
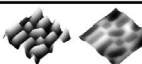
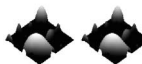

#### IV. Conclusions

Different pathways of rupture, dewetting, and resulting morphologies of thin liquid bilayers are shown by a 3-D long-wave nonlinear analysis. It was found convenient to classify the bilayers according to the macroscopic dewetting behavior of the films. We use a short-range Born repulsion for the van der Waals cutoff to capture detailed dynamics of the true contact lines and elaborate their role in morphological evolution without significant coarsening of structures. A tight summary of the key findings is displayed in Table 1, and the major conclusions are highlighted below.

(i) It is shown that there are several dewetting pathways for the bilayers with unstable lower and upper layers. (A) Cases 2 and 6 show that instability can be initiated by the rupture of any of the films and the initial rupture is dictated by the relative strength of the destabilizing intermolecular forces inside the film. After the first rupture, the dewetting in these two cases propagates by repeated excursions of the upper layer in the lower layer. The final morphologies of *cases 2* and *6* show that the lower layer disintegrates into an array of channels and ridges.



**TABLE 1: Tight Summary of the Results Showing the Short-Time Instability Modes and the Long-Time Dewetted Morphologies**

	Stability Characteristics	Short-Time Modes	Long-Time Dewetted Morphologies (lower film) (upper film)
Case 1 ( $\gamma_s > \gamma_1 > \gamma_2$ )	Both the layers are stable	stable	Flat films
Case 2 ( $\gamma_s > \gamma_2 > \gamma_1$ )	Both the layers are unstable	Squeezing  Bending	
Case 3 ( $\gamma_s < \gamma_1 < \gamma_2$ )	Upper layer is unstable and lower layer is weakly unstable	Squeezing  Bending	 Similar to squeezing
Case 4 ( $\gamma_s < \gamma_2 < \gamma_1$ )	Lower layer is unstable and the upper layer becomes unstable when it comes in contact with the solid	Bending	
Case 5 ( $\gamma_1 > \gamma_s > \gamma_2$ )	Lower layer is unstable and upper layer is stable	Bending	
Case 6 ( $\gamma_2 > \gamma_s > \gamma_1$ )	Both the layers are unstable	Squeezing  Bending	Similar to Case 2  Similar to Case 2

The channels are formed at the places where the lower layer dewets the substrate. The upper layer dewets the lower layer at the ridges formed on the surface of the lower layer and accumulates inside the channels that are formed because of the lower layer dewetting on the solid. (B) In *case 3*, the dewetting is always initiated by the rupture of the upper layer and the weakly unstable lower layer shows an incomplete or “frustrated dewetting” on the solid in congruence with the dewetting of the upper layer. The equilibrium morphology in this case shows the presence of an array of ridges or droplets on the lower layer surface and the upper liquid fills the interstitial spaces around the structures formed on the surface of the lower layer. In this case, the upper layer always rests on a thin cushion of the lower layer because the lower layer never fully dewets the solid surface.

(ii) For a *case 2* system, we have shown that the growth rate of instability becomes faster in the upper layer by reducing its viscous resistance. The final morphology in such a system is entirely different from the systems where the films have similar viscosity. Much of the previous experimental work shows this behavior. Simulations also show that weak deformations of the liquid–liquid interface in this case form a low amplitude replica of the upper interface.

(iii) In *cases 4* and *5*, the instability starts with the rupture of the lower layer first. In *case 4*, the upper layer shows a secondary instability only after the rupture of the lower layer on the solid. The equilibrium contact angle of the dewetted upper layer on the solid is lower than the dewetted lower layer in *case 4*.

Therefore, the three-phase contact line formed of air–upper liquid–solid interface pushes the other three-phase contact line composed of the upper liquid, lower liquid, and solid beyond its equilibrium position. In this process, the upper layer encapsulates the lower layer at the late stages of evolution. In *case 5*, the upper liquid never dewets the solid and traces out the interfacial morphology of the lower layer. The upper liquid descends to fill the gap between droplets of the lower layer, thus leading to an inversion of the top and the bottom phases near the equilibrium. In both cases, the upper layer eventually encapsulates the dewetted structures formed at the lower layer.

In summary, a comprehensive understanding of the instability, dynamics, and morphology of the bilayers is presented based on nonlinear simulations which point to many interesting scenarios in dissipative pattern formation that are of interest in applications ranging from multilayer thin coatings, biological adhesion,<sup>27,28</sup> and self-organized patterning<sup>15–17</sup> to a basic understanding of the pathways of bilayer dewetting.<sup>14,18–26</sup>

**Acknowledgment.** This work was supported by the DST Unit on Nano Science and Technology at IIT Kanpur. Discussions with Prof. Uwe Thiele during this work is gratefully acknowledged.

## References and Notes

- (1) Ruckenstein, E.; Jain, R. K. *J. Chem. Soc., Faraday Trans. 2* **1974**, 70, 132.
- (2) De Gennes, P. G. *Rev. Mod. Phys.* **1985**, 57, 827.
- (3) Brochard-Wyart, F.; Daillant, J. *Can. J. Phys.* **1990**, 68, 1084.

- (4) Brochard-Wyart, F.; Martin, P.; Redon, C. *Langmuir* **1993**, *9*, 3682.
- (5) Reiter, G.; Khanna, R.; Sharma, A. *Phys. Rev. Lett.* **2000**, *85*, 1432.
- (6) Sharma, A.; Jameel, A. T. *J. Colloid Interface Sci.* **1993**, *161*, 190.
- (7) Oron, A.; Davis, S. H.; Bankoff, S. G. *Rev. Mod. Phys.* **1997**, *69*, 931.
- (8) Sharma, A.; Khanna, R. *Phys. Rev. Lett.* **1998**, *81*, 3463.
- (9) Volodin, P.; Kondyurin, A. *J. Phys. D: Appl. Phys.* **1998**, *41*, 065306.
- (10) Oron, A. *Phys. Rev. Lett.* **2000**, *85*, 2108.
- (11) Konnur, R.; Kargupta, K.; Sharma, A. *Phys. Rev. Lett.* **2000**, *84*, 931.
- (12) Saprykin, S.; Trevelyan, P. M. J.; Koopmans, R. J.; Kalliadasis, S. *Phys. Rev. E* **2007**, *75*, 026306.
- (13) Pereira, A.; Trevelyan, P. M. J.; Thiele, U.; Kalliadasis, S. *Phys. Fluids* **2007**, *19*, 112102.
- (14) Higgins, A. M.; Jones, R. A. L. *Nature* **2000**, *404*, 476.
- (15) Lin, Z. Q.; Kerle, T.; Baker, S. M.; Hoagland, D. A.; Schaffer, E.; Steiner, U.; Russell, T. P. *J. Chem. Phys.* **2001**, *114*, 2377.
- (16) Lin, Z. Q.; Kerle, T.; Russell, T. P.; Schaffer, E.; Steiner, U. *Macromolecules* **2002**, *35*, 3971.
- (17) Lin, Z. Q.; Kerle, T.; Russell, T. P.; Schaffer, E.; Steiner, U. *Macromolecules* **2002**, *35*, 6255.
- (18) Lambooy, P.; Phelan, K. C.; Haugg, O.; Krausch, G. *Phys. Rev. Lett.* **1996**, *76*, 1110.
- (19) Pan, Q.; Winey, I. K.; Hu, H. H.; Composto, R. J. *Langmuir* **1997**, *13*, 1758.
- (20) Segalman, R. A.; Green, P. F. *Macromolecules* **1999**, *32*, 801.
- (21) Wang, C.; Krausch, G.; Geoghegan, M. *Langmuir* **2001**, *17*, 6269.
- (22) Kang, H.; Lee, S. H.; Kim, S.; Char, K. *Macromolecules* **2003**, *36*, 8579.
- (23) Wunnicke, O.; Muller-Buschbaum, P.; Wolkenhauer, M.; Lorenz-Haas, C.; Cubitt, R.; Leiner, V.; Stamm, M. *Langmuir* **2003**, *19*, 8511.
- (24) de Silva, J. P.; Geoghegan, M.; Higgins, A. M.; Krausch, G.; David, M. O.; Reiter, G. *Phys. Rev. Lett.* **2007**, *98*, 267802.
- (25) Li, Y.; Yang, Y.; Yu, F.; Dong, L. *J. Polym. Sci., Part B: Polym. Phys.* **2006**, *44*, 9.
- (26) Julien LeOpolde, S.; Damman, P. *Nat. Mater.* **2006**, *5*, 957.
- (27) de Souza, E. R.; Gallez, D. *Phys. Fluids* **1998**, *10*, 1804.
- (28) Coakley, W. T.; Gallez, D.; de Souza, E. R.; Gauci, H. *Biophys. J.* **1990**, *77*, 817.
- (29) Maldarelli, C. H.; Jain, R. K.; Ivanov, I. B.; Ruckenstein, E. *J. Colloid Interface Sci.* **1980**, *78*, 118.
- (30) Danov, K. D.; Paunov, V. N.; Alleborn, N.; Raszillier, H.; Durst, F. *Chem. Eng. Sci.* **1998**, *53*, 2809.
- (31) Danov, K. D.; Paunov, V. N.; Stoyanov, S. D.; Alleborn, N.; Raszillier, H.; Durst, F. *Chem. Eng. Sci.* **1998**, *53*, 2823.
- (32) Paunov, V. N.; Danov, K. D.; Alleborn, N.; Raszillier, H.; Durst, F. *Chem. Eng. Sci.* **1998**, *53*, 2839.
- (33) Bandyopadhyay, D. M. Tech. Thesis, Indian Institute of Technology, Kanpur, India, 2001.
- (34) Paunov, A.; Bestehorn, M.; Merkt, D.; Thiele, U. *Phys. Rev. E* **2004**, *70*, 025201.
- (35) Bandyopadhyay, D.; Gulabani, R.; Sharma, A. *Ind. Eng. Chem. Res.* **2005**, *44*, 1259–1272.
- (36) Pototsky, A.; Bestehorn, M.; Merkt, D.; Thiele, U. *J. Chem. Phys.* **2005**, *122*, 224711.
- (37) Fisher, L. S.; Golovin, A. A. *J. Colloid Interface Sci.* **2005**, *291*, 515.
- (38) Bandyopadhyay, D.; Sharma, A. *J. Chem. Phys.* **2006**, *125*, 054711.
- (39) Pototsky, A.; Bestehorn, M.; Merkt, D.; Thiele, U. *Europhys. Lett.* **2006**, *74*, 665.
- (40) Merkt, D.; Pototsky, A.; Bestehorn, M.; Thiele, U. *Phys. Fluids* **2005**, *17*, 064104.
- (41) Nepomnyashchy, A. A.; Simanovskii, I. B. *Phys. Fluids* **2006**, *18*, 112101.
- (42) Nepomnyashchy, A. A.; Simanovskii, I. B. *Phys. Fluids* **2006**, *18*, 032105.
- (43) Kumar, S.; Matar, O. K. *J. Colloid Interface Sci.* **2004**, *273*, 581.
- (44) Matar, O. K.; Gkanis, V.; Kumar, S. *J. Colloid Interface Sci.* **2005**, *286*, 319.
- (45) Fisher, L. S.; Golovin, A. A. *J. Colloid Interface Sci.* **2007**, *307*, 203.
- (46) Lenz, R. D.; Kumar, S. *J. Colloid Interface Sci.* **2007**, *316*, 660.
- (47) Israelachvili, J. N. *Intermolecular and Surface Forces*; Academic Press: London, 1992.
- (48) van Oss, C. J.; Chaudhury, M. K.; Good, R. J. *Chem. Rev.* **1988**, *88*, 927.
- (49) Khanna, R.; Sharma, A. *J. Colloid Interface Sci.* **1997**, *195*, 42.
- (50) Ghatak, A.; Khanna, R.; Sharma, A. *J. Colloid Interface Sci.* **1999**, *212*, 483.
- (51) Oron, A.; Bankoff, S. G. *J. Colloid Interface Sci.* **1999**, *218*, 152.